Supplementary material of "Remote hydrological control on crustal seismicity" by Pintori F. et al.

S1 Geodetic analysis

S.1.1 GNSS dataset and data processing

The position time-series have been obtained adopting a three-step procedure approach, as in Serpelloni et al. (2006), that includes: 1) raw phase data reduction, 2) combination of loosely constrained network solutions and reference frame definition and 3) time-series analysis, including velocity estimates and spatial filtering of common mode errors.

The raw GPS observables have been analyzed using the 10.70 version of the GAMIT/GLOBK package (Herring et al., 2018) adopting standards defined in the framework of the IGS "Repro2 campaign" (http://acc.igs.org/reprocess2.html). The GAMIT software is used to estimate station positions, atmospheric delays, satellite orbits, and Earth orientation parameters from ionosphere-free linear combination GPS phase observables using double differencing techniques to eliminate phase biases caused by drifts in the satellite and receiver clock oscillators. GPS pseudo-range observables are used to constrain clock timing offsets and to improve automated editing of the phase data, assisting in the resolution of integer phase ambiguities. GPS phase data are weighted according to an elevation-angle-dependent error model (Herring et al., 2015) using an iterative analysis procedure whereby the elevation dependence is determined from the observed scatter of phase residuals. In this analysis the satellites orbit parameters are tightly constrained to the IGS final products. We use the IGS absolute antenna phase center model for both satellite and ground-based antennas, which improves the accuracy of estimates for the vertical components of site position by mitigating reference frame scale and atmospheric mapping function errors (Schmid et al., 2005; 2007). While the first-order ionospheric delay is eliminated by the ionosphere-free linear combination, the second-order ionospheric corrections are applied based on the formulation of (Petrie et al., 2010), using IONEX files from the Center for Orbit Determination in Europe (CODE). The tropospheric delay is modeled as piecewise linear model and estimated using the Vienna Mapping Function 1 (VMF1; Boehm et al., 2007) with a 10° cutoff. We use the Global Pressure and Temperature 2 (GPT2; Lagler et al., 2013) model to provide a priori hydrostatic delays. The pole tide was also corrected in GAMIT by IERS standards. The Earth Orientation Parameters (EOP) are tightly constrained to priori values obtained from IERS Bulletin B. Non-tidal atmospheric loading and ocean tidal loading are corrected using MIT filtered atmospheric displacements files (available at ftp://everest.mit.edu/pub/GRIDS) and the FES2004 (Lyard et al., 2006) model, respectively. The International Earth Rotation Service (IERS) 2003 model for diurnal and semi-diurnal solid Earth tides was set. Because of the large number of stations included in our Euro-Mediterranean GPS processing (~3000), this step is performed for several sub-networks, each made by <50 stations, with each sub-network sharing a set of high-quality IGS stations, which are used as tie-stations in the combination step.

In the second step we use the ST_FILTER program of the QOCA software (http://qoca.jpl.nasa.gov), which adopts a Kalman filter estimation algorithm (Dong et al., 1998; 2002), to combine all the daily loosely constrained solutions with the global solution of the IGS network made available by MIT (http://sopac.ucsd.edu), and simultaneously realize a global reference frame by applying generalized constraints (Dong et al., 1998). Specifically, we define the reference frame by minimizing the velocities of the IGS core stations (http://igscb.jpl.nasa.gov), while estimating a seven- parameter transformation with respect to the GPS realization of the ITRF2008 frame (Altamimi et al., 2011), i.e., the IGb08 reference frame.

In the third step we analyze the position time series in order to estimate and correct offsets due to stations equipment changes, while simultaneously estimating annual and semi-annual periodic signals and a linear velocity term. The model derived from the combination of these signals is then subtracted from the position time series in order to get the residual positions. The residual time-series are then used to estimate the Common Mode Error (CME) performing a Principal Component Analysis (PCA), as described in Dong et al. (2006). The PCA is performed at a continental-scale, over the same area used by Serpelloni et al. (2013), and the first two PCs are here considered as CME. This prevents the removal of the eventual more localized signals of geophysical interests recorded by the GPS stations in the study region, since the PCA detects the signals common to a much larger region. As a result, after removing the CME, the typical repeatability in our analysis is ~1 mm for the horizontal components, and ~3 mm for the vertical component, with a 30% gain in the daily repeatability and a significant improvement of the signal to noise ratio. After the spatial filtering, the estimated seasonal motions are added back to the filtered time-series, obtaining position time series with a reduced scatter around the adopted model. The filtered displacement time-series are rotated in a Adria-fixed reference frame using the rotation pole parameter estimated from GPS velocities in Serpelloni et al. (2016).

S1.2 Description of the procedure used to remove the linear trend using vbICA

We applied a vbICA (Gualandi et al., 2016) to the GPS time series in the Adria-fixed reference frame. Through this process, the displacement time-series of the GPS stations are decomposed into a finite number of independent components (ICs), characterized by a spatial distribution (U), a temporal evolution (V) and a weight coefficient (S). As shown by Gualandi et al. (2016), the number of ICs used to decompose the observations must be chosen *a-priori*, and in order to decide on the number of components to retain several statistical tests can be applied. In this work we use the F-test.

The component that describes the largest variance of the dataset is IC1, which we interpret as the linear tectonic trend (Fig. S1.2a), to which a sinusoidal annual signal is superimposed. The presence of an annual signal in the component representing the tectonic trend is due to the fact that ICA is not able to completely separate the tectonic

3

signal from other processes. Assuming that the tectonic trend is linear, we initially estimate it by fitting the temporal evolution of IC1 with the following function:

$$q+m\cdot x+A\cdot\sin\left(2\pi\cdot x+\varphi\right) \tag{S1}$$

and considering only the terms

$$V_{lin}=q+m\cdot x \tag{S2}$$

Since the displacements reconstructed by the IC1 are $V_1\cdot S_1\cdot U_1$, where S_1 is the weight coefficient and U_1 the spatial distribution, the displacements associated only with the linear trend of IC1 are $V_{lin}\cdot S_1\cdot U_1$.

It is then possible to remove this component of the displacement ($V_{lin}\cdot S_1\cdot U_1$) from the displacement time series and then apply another vbICA to the new detrended time-series. This approach is effective in detrending short spanning time-series of GNSS stations affected by transient displacements, where a trajectory model (Bevis and Brown, 2014) would fail if the transient is not properly modeled with an *ad hoc* function.

We remark that the values of both *q* and *m* are slightly affected by both the number of components chosen for the ICA, in particular when considering 4 ICs or more, and the initial decomposition parameters. Since once removed the linear trend, 3 components are necessary to reconstruct the observations according to the F-test, then we selected 4 ICs for the decomposition of the signal in the Adria-fixed reference frame (Fig. S1.2): one more than the detrended case, representing the tectonic motion.

4

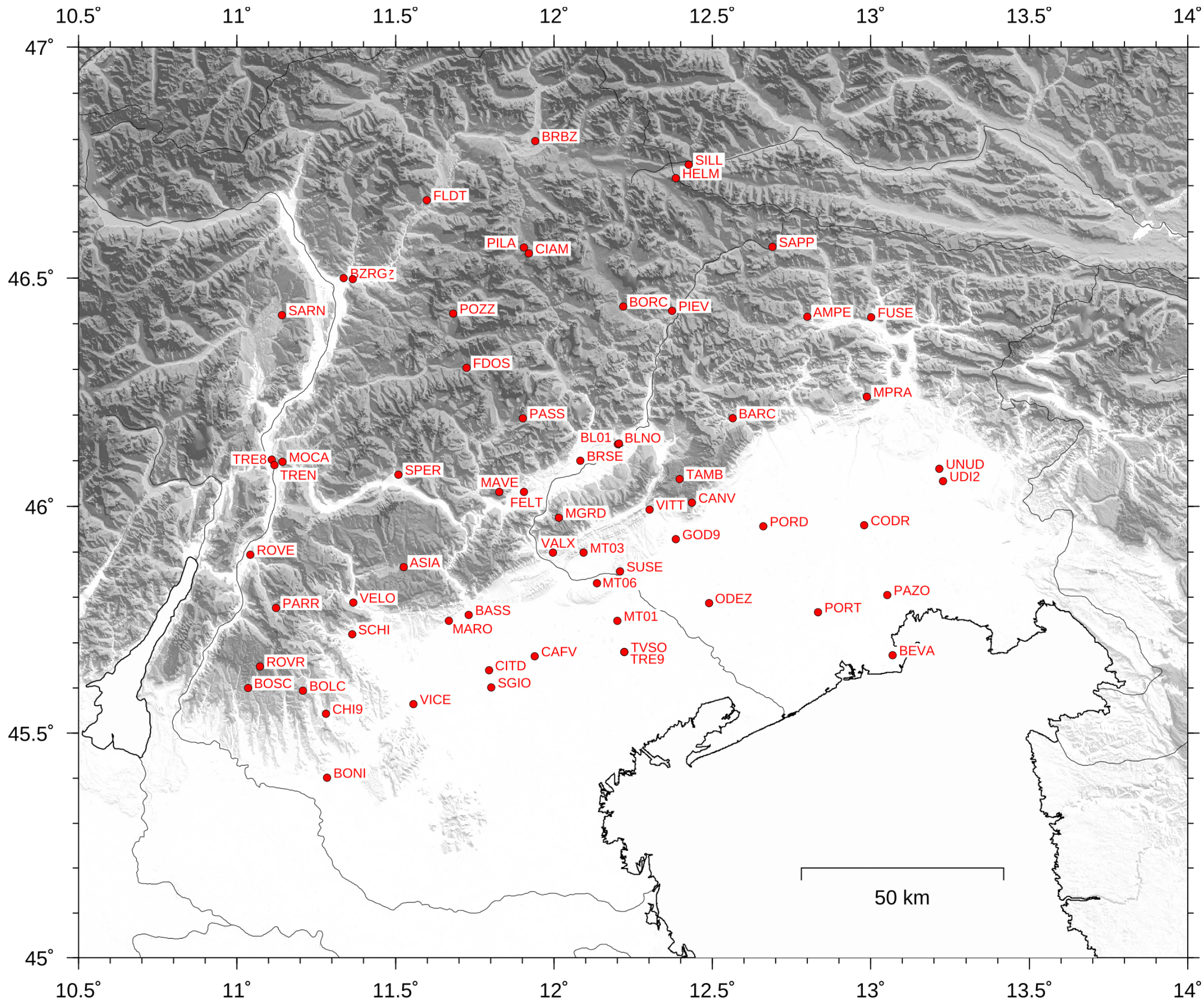

Figure S1.1. Map of the GPS stations included in the vbICA analysis.

5

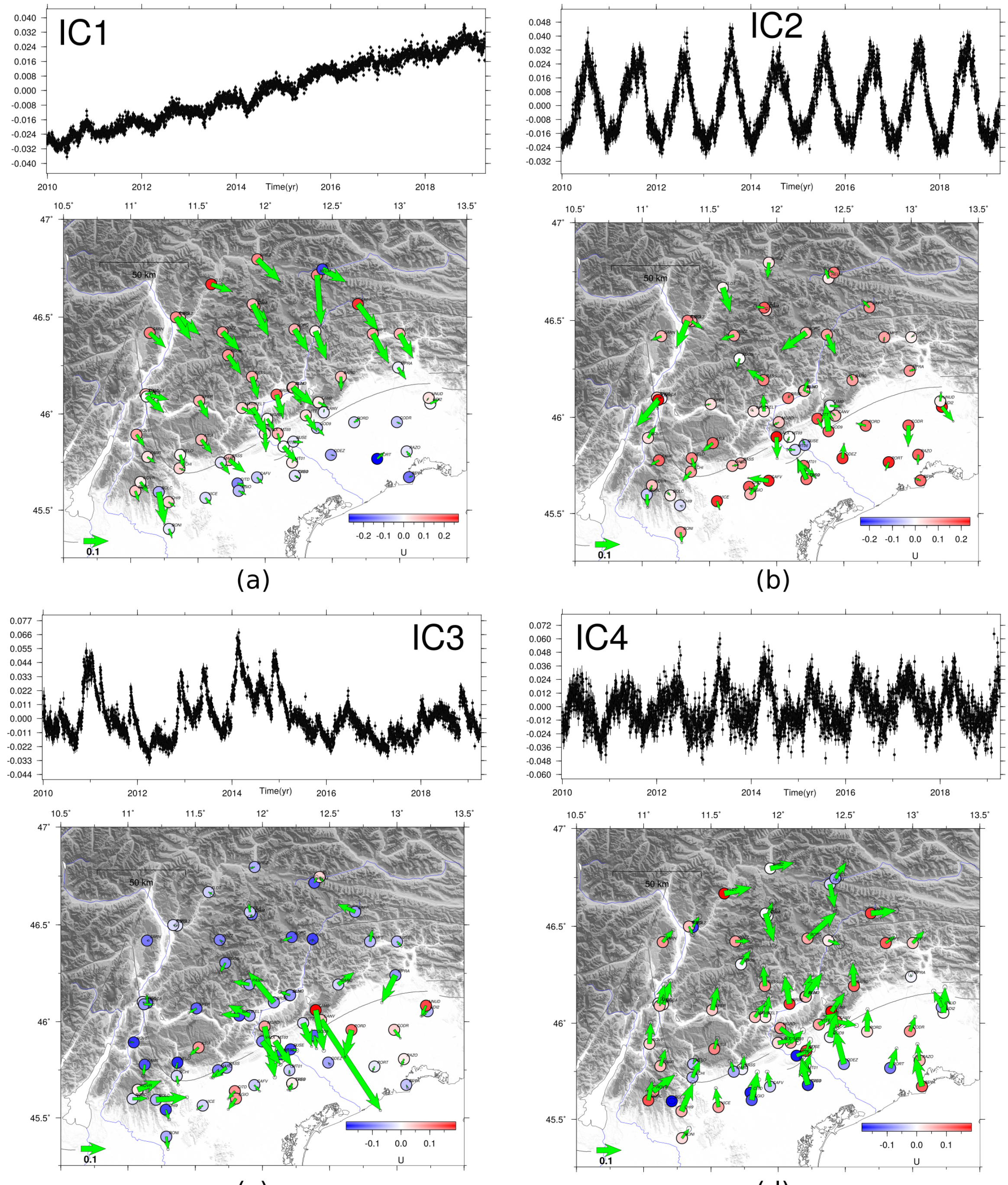

Figure S1.2. Result of the vbICA analysis using GNSS time series in the Adria-fixed reference frame. The (a), (b), (c), (d) panels represent IC1, IC2, IC3, IC4 respectively. The top of each panel represents the temporal evolution (V; in black), while in the map is plotted the corresponding spatial response in the horizontal (green arrows) and vertical (coloured circles) components. As regard IC1, the directions and amplitudes of the spatial response are in good agreement with horizontal and vertical velocities estimated with the classic trajectory model approach of Anderlini et al. (2020).

 6

S2 Hydrological modeling

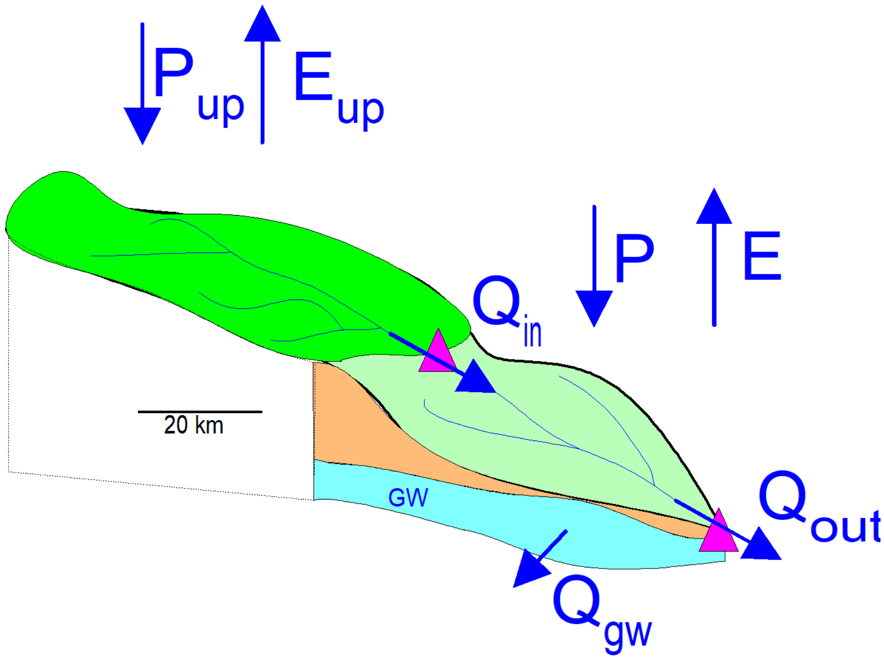

Figure S2.1. Schematic describing the modeling approach to estimate total water storage changes in a downstream sub-catchment (light green), based on precipitation (P), actual evapotranspiration (E), river discharge (Qin and Qout), and potential groundwater import/export from a surrounding basin Qgw (e.g. karstic system).

S2.1. Spatially-distributed precipitation and temperature

As the single water flux increasing storage changes, an adequate estimation of precipitation is required to robustly quantify them. Since rainfall is highly heterogeneous over this mountainous region, we considered 54 pluviometers and 55 temperature observations distributed within or close to the Piave at Segusino catchment (Fig. S2.2). Data are available from 2010 to present.

We used the Thiessen polygons (i.e. nearest neighbour method) to compute mean rainfall over each of the three catchments. This method consists in dividing the entire basin in Thiessen polygons generated from a set of sample points, which in the case of precipitation

 7

estimation are the pluviometers. Each polygon has the property of the closest pluviometer. Note that the shape of the Thiessen might evolve over time to account for potential missing data.

Assuming that inside (or very close to) the hydrological basin we are considering there are n pluviometers, the weighted mean precipitation (P_m) at certain time is computed as follows:

$$P_m = \frac{\sum_{i=1}^{n} p_i A_i}{\sum_{i=1}^{n} A_i} \qquad \text{(S3)}$$

where p_i is the precipitation recorded by the i-th pluviometer and A_i the area of the polygon it represents. The time resolution of the data we are using is daily, then P_n is daily too.

This computation process can be complicated by the presence of missing data and by the fact that the calculus of polygon areas is not that easy. Then, in order to compute the areas of Thiessen polygons, we build a grid with squared cells over the basin with a resolution of 2 km both in the N-S and E-W direction, and count how many grid cells points (at the corners of each cell) lie inside each polygon: the larger the polygon is the more points are inside it (Fig. S2.2). In this way A_i in equation (S3) becomes the number of points that are inside the i-th polygon.

In order to compute the mean temperature of the area we follow the same process, using as sample points the position of the thermometers.

8

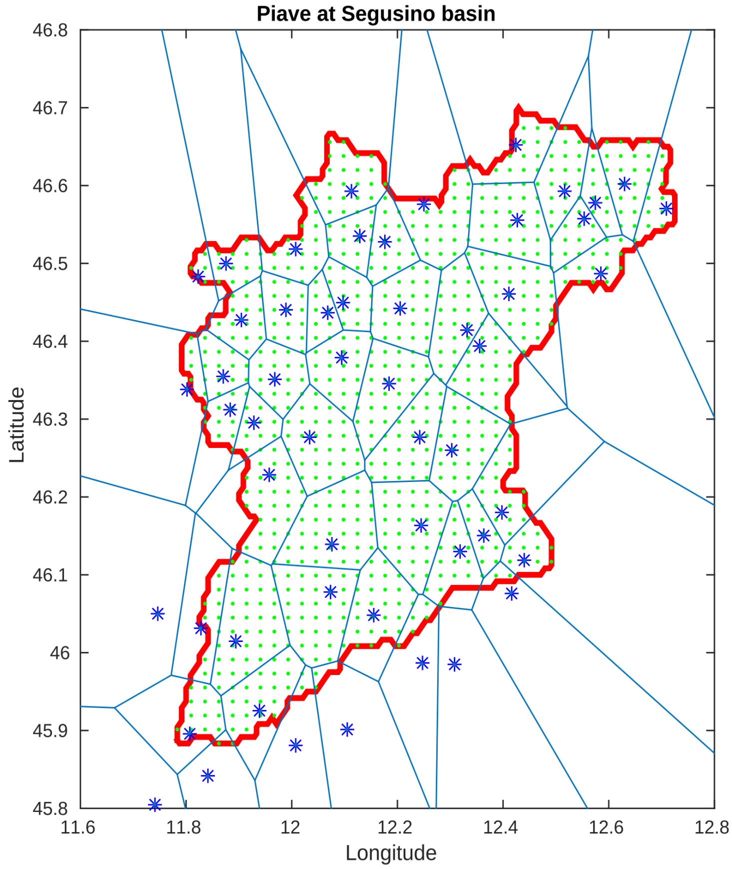

Figure S2.2. Example of division of the Piave at Segusino basin (red line) in Thiessen polygons (blue lines) to compute mean precipitation. The blue stars represent the pluviometers that generate the Thiessen polygons, while the small green dots inside the basin are the grid points we used to compute A_i.

S2.2. Potential evapotranspiration

Actual evapotranspiration E is first estimated based on potential evapotranspiration (PET) - i.e. the atmospheric demand for moisture. We used the Jensen-Haise (Jensen et al. 1990) method to estimate PET:

$$PET = \frac{R_e(T+5)}{100\,\lambda\,\rho} \text{ if } T+5>0;\ PET=0 \text{ otherwise} \qquad \text{(S4)}$$

This approach only requires a limited amount of information, temperature (T) and

9

extraterrestrial radiation (R_e), depending only on latitude and julian day. $\lambda = 2.45\frac{MJ}{Kg}$ is the latent heat flux and $\rho = 1000\frac{Kg}{m^3}$ is the density of water. As underlined by (Oudin et al., 2005), such a simplified model, which is based on local observations, does not affect the model performances.

S2.3. Modeling water storage changes with GR5J hydrological model (Belluno Valley, 883 km²)

We used the catchment-scale GR5J rainfall-runoff model (Pushpalatha et al., 2011) to compute water balance and total water storage changes at daily time steps. Although the model is conceptual and simplified, it has proven skillful in predicting river discharge better than more complex models (de Lavenne et al., 2016) and has been successfully applied to represent groundwater storage changes in Nepal rivers (Andermann et al., 2012). The model parsimony is considered here as a strength considering the limited information available to define actual flow and storage processes in the karst area investigated. One important feature of GR5J is the possibility to describe subsurface water exchanges with surrounding basins, as expected in karst regions. The model is driven by P and PET, and finally calibrated on observed river discharge using a Marquard-Levenberg least-square approach on the logarithm of water discharge to limit the impact of floods and promote the description of the whole water cycle.

The quality of the model is evaluated using the Nash-Sutcliffe efficiency (Nash and Sutcliffe, 1970). This normalized index can range from $-\infty$ to 1. An efficiency of 1 corresponds to a perfect description of observed discharge. When the efficiency falls to 0, model predictions are as accurate as the mean of the observed data. GR5J performs quite well on the 3 catchments (Table S2.1).

10

Watershed	Catchment area [km²]	Nash-Sutcliffe efficiency	Correlation between modeled water storage changes and ICA V2 eigenvector
Cordevole@ Ponte Mas	706	0.62	0.78
Piave@ Belluno	1907	0.72	0.84
Piave@ Segusino	3496	0.76	0.88
Belluno Valley	883	N/A	0.84
GRACE	$\sim 10^5$	N/A	0.61
GLDAS	3496	N/A	0.18

Table S2.1. Nash-Sutcliffe efficiency coefficient and correlation with V2 for the basins considered.

Total water storage [m^3] is computed for each of the 3 watersheds with the GR5J model as the sum of storage in the different compartments multiplied by the area of the catchment. As the Belluno Valley is localized between two upstream river discharge stations (Piave at Belluno, Cordevole at Ponte Mas) and the downstream station (Piave at Segusino), GR5J model is first calibrated on each catchment. Belluno Valley water storage changes are computed as the difference between storage changes within the Piave at Segusino catchment, minus storage changes within the upstream catchments (Fig. S2.1)

For all basins, water storage changes are highly correlated with the temporal variations in surface displacements, as described by the second eigenvector of ICA (Fig. S2.3), around or above 0.8. The correlation between V2 and TWS is high during all the time interval, implying that not only the large deformation events, but also the small ones are well modeled. One exception is the extreme weather event, named “tempesta Vaia”, occurred at the end of October 2018, where the increase of the V2 is smaller than the TWS. The reason might be that, during this event, the precipitation in the northern sector of the basins was much higher than in the southern one, where the GPS stations responding to this hydrological signal are located. This is confirmed by Fig. 4 and Fig. S2.3, where the TWS peak during the Vaia storm computed in the Belluno Valley catchment basin is much smaller than in the river basins.

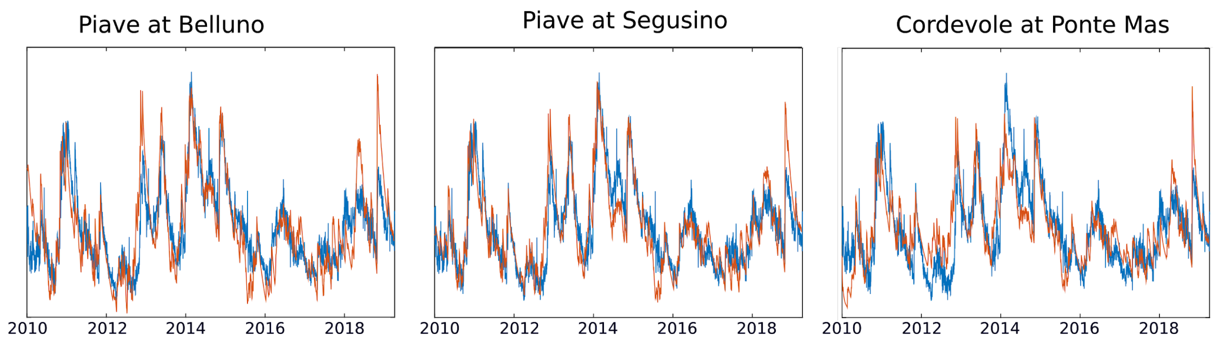

Figure S2.3. Comparison between V2 (blue) and TWS variations (red) computed in the Piave at Belluno (left), Piave at Segusino (center) and Cordevole at Ponte Mas (right).

S2.4. Large-scale storage changes

Large-scale model outputs are generally used to estimate water storage changes, computed as the sum of all storage compartments. Such models are not suited to describe the behavior of the catchment, considering that lateral flow is generally not taken into account .

In this paragraph we consider water storage changes modeled by GRACE and GLDAS, and compare them with V2. In particular, we used gridded monthly global water storage changes derived from GRACE and GRACE-FO and processed at JPL using the Mascon approach (Version2/RL06, https://grace.jpl.nasa.gov/data/get-data/jpl_global_mascons/) in

12

a rectangular area with limits: Lon. 11°- 13°; Lat. 45.5°- 46.5°. We also take into consideration the superficial water content estimated by GLDAS Noah (Rodell, 2016; *GLDAS Noah Land Surface Model L4 monthly 0.25 x 0.25 degree V2.1 (GLDAS_NOAH025_M) at GES DISC*) in the Piave at Segusino basin, as the mean soil moisture plus the mean snow depth water equivalent up to 2m depth.

It is worth noting that the spatial integration of GRACE (>100 000 km²) is much wider than the area of the studied basins (~1000 km²); while the GLDAS spatial resolution is 0.25°x0.25°. Both datasets are monthly.

We observe that GRACE and GLDAS TWS changes estimations are much seasonal than V2 and TWS computed in the basins through GR5J (Fig. S2.3; S2.5), while the typical dynamic in flow is much faster.

13

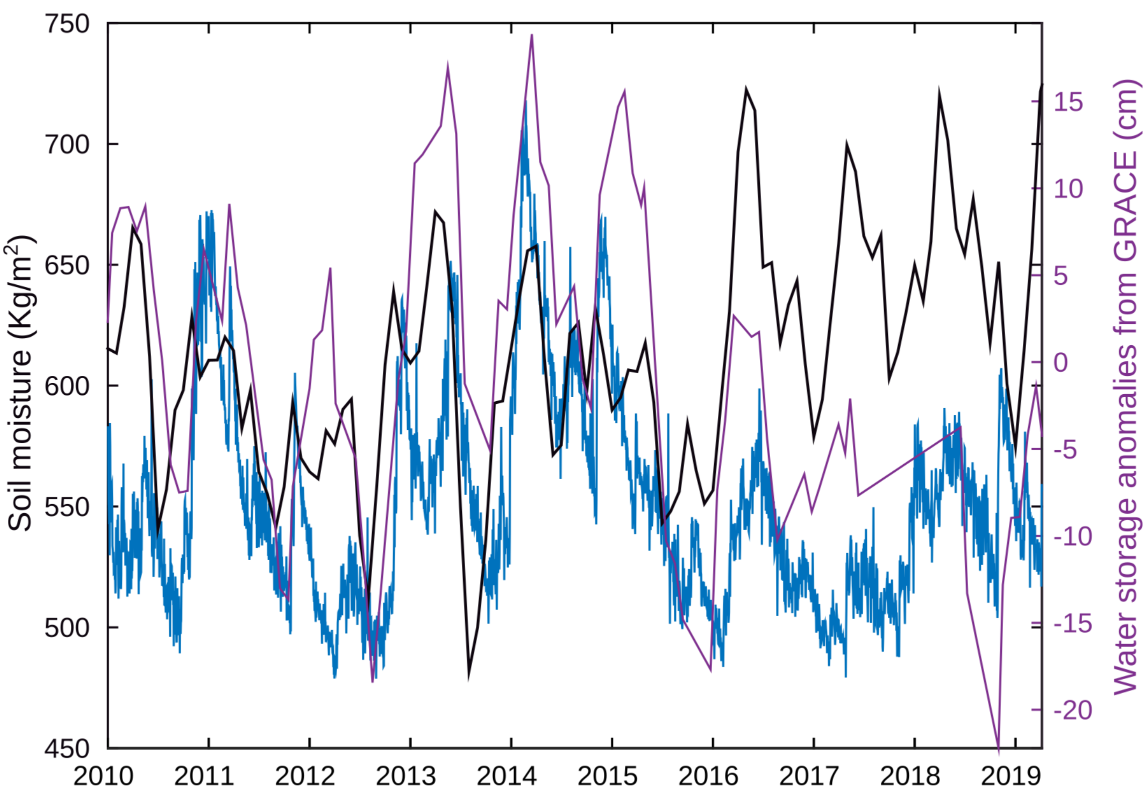

Figure S2.4. Blue: V2; black: mean soil moisture plus mean snow depth water equivalent computed by GLDAS Noah (*GLDAS Noah Land Surface Model L4 monthly 0.25 x 0.25 degree V2.1 (GLDAS_NOAH025_M) at GES DISC*) up to 2m depth (purple) in the Piave at Segusino basin; purple: mean water storage anomalies (equivalent water thickness units [cm]) relative to a time-mean, derived from GRACE and GRACE-FO and processed at JPL using the Mascon approach (Version2/RL06). We consider a rectangular area with limits Lon: 11°- 13°; Lat: 45.5°- 46.5°.

14

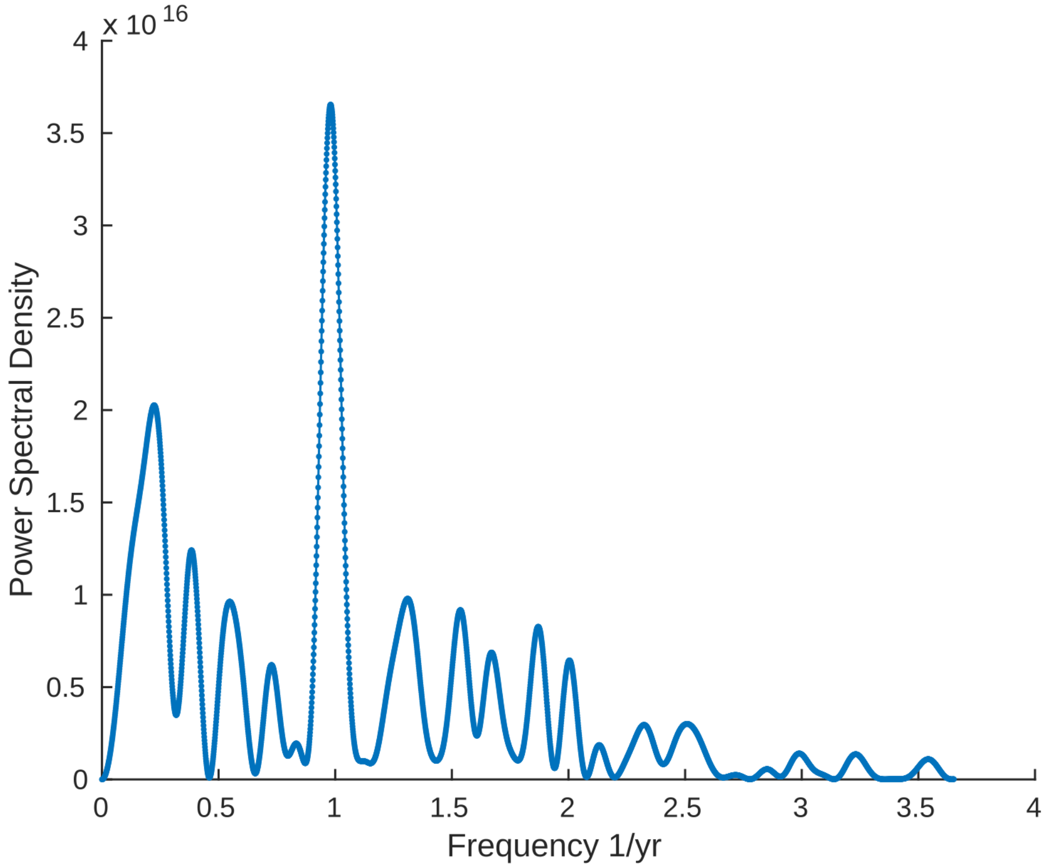

Figure S2.5. Power spectral density of TWS_{res}.

S3 Hydro-mechanical modeling

S3.1. Modeling displacements and stress changes

We used a finite element model (FEM) in order to explore physical linkages between water storage changes in the Belluno Valley and surface deformation recorded by GNSS stations, and compute subsurface stress variations. We define a geologically realistic model and test a set of hydrological structures that could explain the observed surface displacements.

In order to focus on physical processes linking the hydrological cycle and deformation, the problem was reduced to 2-D under the plane strain hypothesis, where linear elasticity is resolved considering small deformations. The modeled domain is 1000 x 500 km, i.e. 200

 15

time wider than the area of interest to avoid boundary effects. The chosen boundary conditions are fixed constraints in the lateral and bottom edges, free surface on the top edge (Fig. S3.1). The mesh is triangular with 20 m size near the boundaries. The size of the domain and the associated mesh were determined as the best compromise between stability and accuracy of the deformed domain and the calculation time. The FEM is performed with Comsol Multiphysics (https://www.comsol.com/).

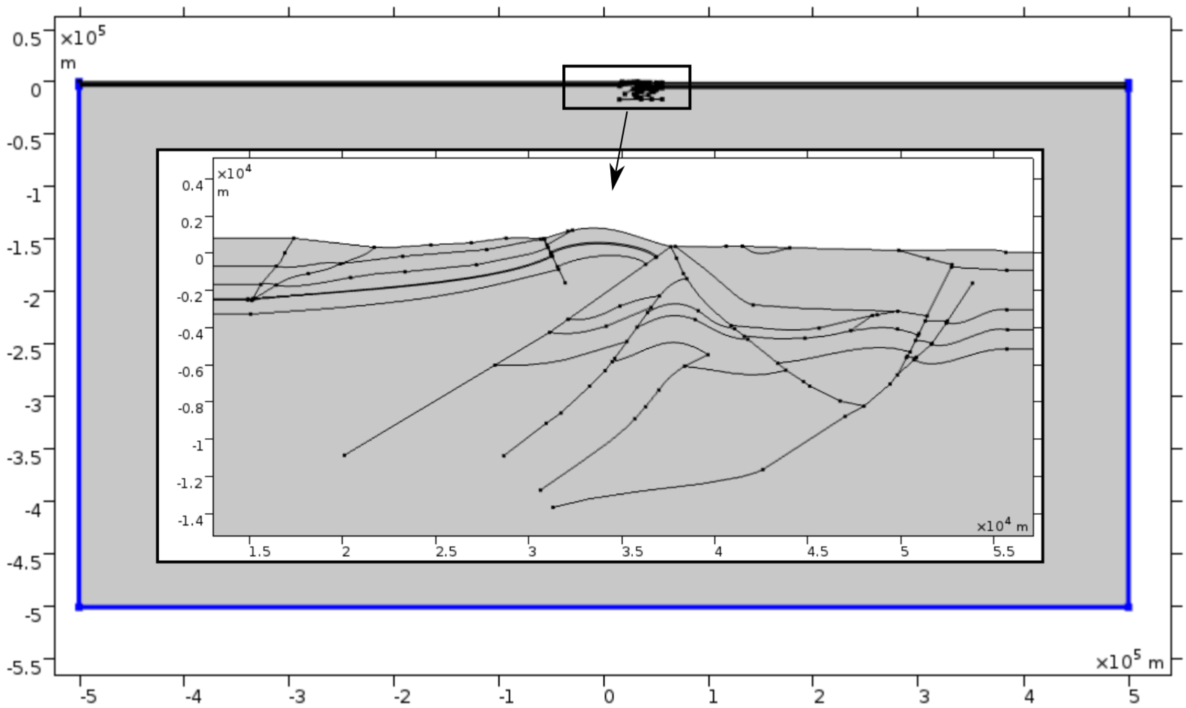

Figure S3.1. Entire domain of the COMSOL model, in blue the fixed constraint. In the black rectangle a closer look to the modeled study area.

The definition of the model is based on the geological cross section shown in Fig. 5 of the main text (from Galadini et al., 2005), where the main geological units are explicitly described. Each layer is considered as elastic, homogeneous and isotropic. We considered perfect continuity between the different layers. No specific elastic behavior was considered for the faults following the small deformation hypothesis. Elastic parameters attributed to the different formations, according to Anselmi et al. (2011), are highlighted in Table S3.1.

16

Rock type	Young’s modulus [GPa]	Poisson’s ratio
Crystalline basement	92	0.25
Belluno Basin Units	59	0.26
Igne Formation	64	0.3
Flysch	26	0.2
Scaglia Rossa	38	0.3
Dolomites	95	0.32
Montello Conglomerates	26	0.2
Limestones	71	0.25
Sediments	15	0.35

Table S3.1. Rock parameters used in COMSOL.

S3.2. Testing hydrological pressure sources to explain surface displacements

In this section we illustrate the different models we tested in order to describe the relationship between TWS_{res} changes and the displacements associated with IC2 in a specific time-span. We assume that the pressure variations caused by the accumulation of water are directly proportional to the TWS_{res} changes.

As deformation is linear with pressure, the different mechanical models are evaluated on the ability of reproducing the spatial distribution of relative surface displacements extracted from IC2. In this way, the mechanical model remains independent from any hydrological model. Noise levels are also considered in the evaluation. It is worth noting that the vertical displacements associated with IC2 are noisier than the horizontal ones, as shown in Fig. S3.3, so that the analysis of the model performance is mainly driven by the horizontal displacements. In particular, when considering the vertical displacements associated with IC2 during T1 (October 10th, 2013 - February 22nd, 2014), 11 of the 12 stations considered have a value smaller than the mean noise level, which is, for each GPS station, the mean error associated with the daily measurements. The model displacements, for each configuration, are shown in Fig. S3.2.

Here is the list of the models, shown in Fig. 6 of the main text:

Model 1: water is hosted in the most permeable karst aquifer above the Igne formation, so that water storage changes translates into pressure changes, and applied vertically on the aquiclude**.** Predicted vertical displacements are generally consistent in sign with the observations (Fig. S3.2). On the contrary, horizontal displacements are for most stations opposite in sign compared to observations: compressional deformation is generated instead of an extension.

Model 2a: similar to Model 1, but considering that groundwater levels are much lower, water storage change is focused in the north sector of the anticline, considering the Bassano-Valdobbiadene backthrust as an aquiclude**.** In this model water does not accumulate in all the portion of the interface between the Igne formation and the Belluno Basin Units, as assumed in Model 1. Similar to Model 1, predicted horizontal displacements are in all cases in the opposite sense than the IC2-reconstructed ones. Modeled vertical displacements are, with the exclusion of MGRD, in the opposite sense.

Model 2b: similar to Model 2a, considering the Bassano-Valdobbiadene thrust as an aquiclude. Modeled displacement patterns are similar to Model 2a, with the exception that horizontal displacement at MGRD is in agreement with observations.

Model 2c: the combination of 2a and 2b. Also in this case the displacement pattern is not well described.

Model 3: water storage changes is stored within the the Belluno Valley, so that water pressure is applied vertically at the surface. While modeled vertical displacements, excluding MGRD, are consistent in sign with observations, horizontal displacements provide a compressional behavior.

Model 4: the damage zone of the Bassano-Valdobbiadene thrust is considered as highly permeable down to depths where it intersects the impermeable Igne formation. Water storage changes translates into pressure changes, which is applied orthogonal to the

18

fracture walls. Pressure is defined following Longuevergne et al. (2009): considering h0 the initial water height in the fracture, and h1 the new height following water level change, P pressure on the fracture walls is constant from the bottom of the fracture up to h0 and equals P=rho*g*(h1-h0) where rho is the water density and g the gravity acceleration. In the portion of the fracture above h0, the pressure increase on the walls is triangular depends on the water level elevation (h) so that P=rho*g*(h1-h). Modeled horizontal displacements matches the observations, except for MGRD station. Vertical displacements are also in good agreement.

Model 5: similar to Model 4, the open fractured network associated with Bassano-Valdobbiadene backthrust is considered as permeable**.** Unlike Model 4, all modeled horizontal displacements are well reproduced, including MGRD station.

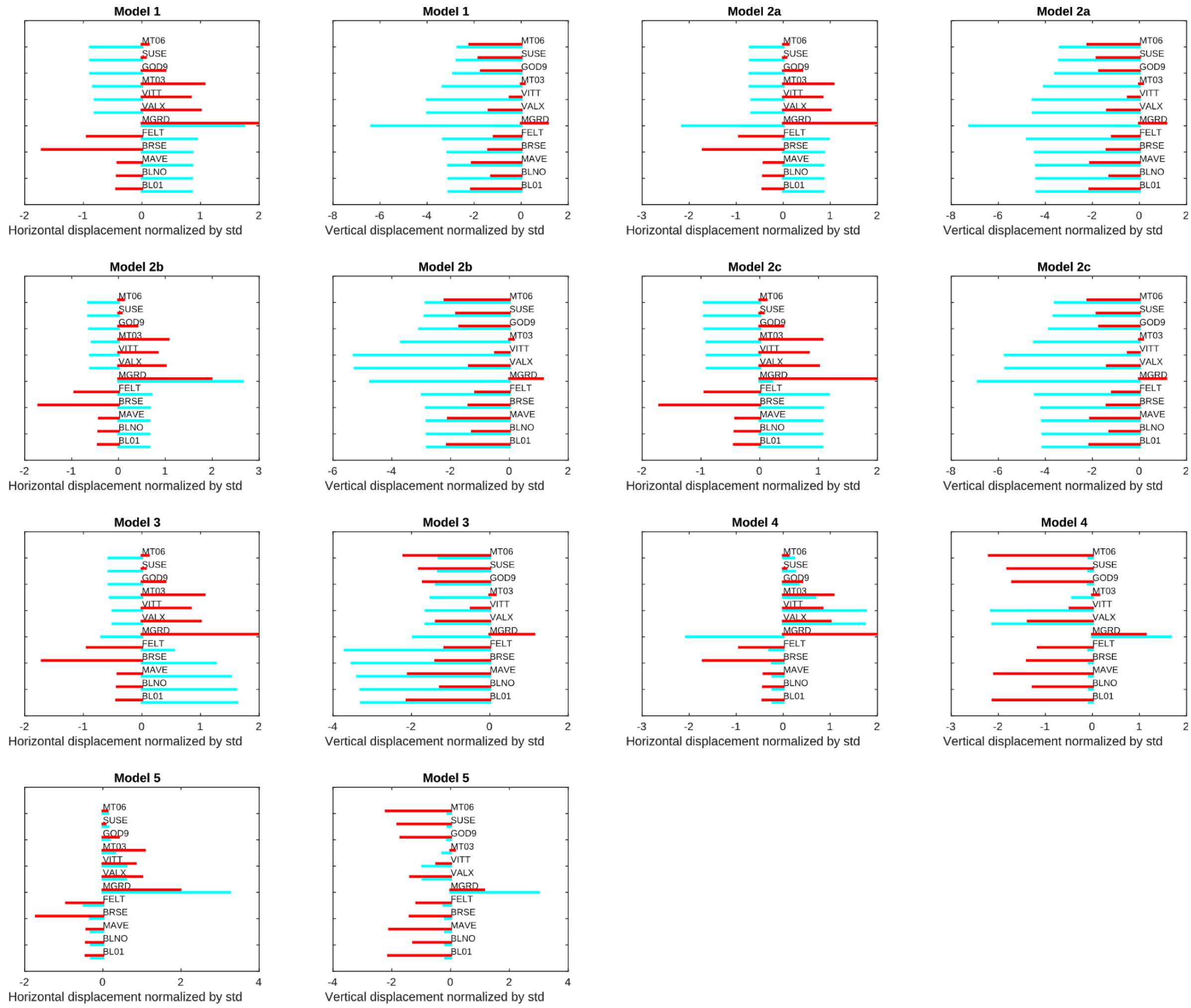

Figure S3.2. Comparison between displacements associated with IC2 during T1 (red) and modeled using COMSOL using 7 different sources of deformation (blue). In order to better compare the displacement patterns, both horizontal and vertical displacements have been normalized with their standard deviation.

The ability of the mechanical models to reproduce IC2 is synthetized on a 2-axis plot representing the ratio of horizontal and vertical displacements *versus* a good description of the spatial pattern of displacements (Fig. S3.3). The y axis represents the ratio between the mean absolute vertical and horizontal displacements, while the x axis the number of stations on which the displacement sign agrees with IC2. The blue diamond “ICA” represents the result of the IC2 reconstruction; the closer a model is to ICA diamond, the better performs. The distance between “loading” scenarios *versus* the “fracture” scenarios are clearly highlighted on this diagram, as expected from their relative behavior in generating extensional horizontal displacements for increasing water storage changes. Fracture type pressurization is required to describe observations, and model 5 is preferred.

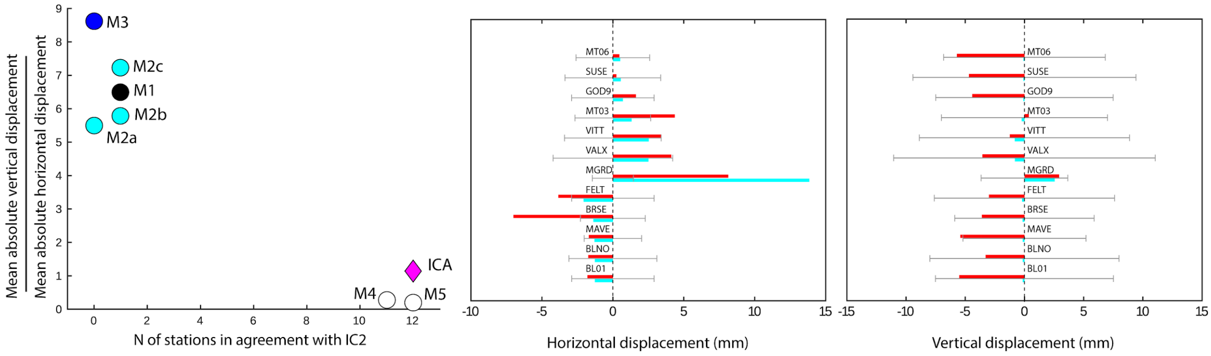

Figure S3.3. Left: Bi-objective plot describing model ability to describe observations. In the y axis the ratio between the norm of the vertical and the horizontal displacement; in the x axis the number of stations with the horizontal displacement pattern in agreement in sign with IC2. Center and right: horizontal (along N21.5°W direction) and vertical displacements, reconstructed during T1 period (see Fig. 1) by IC2 (red) and computed by the numerical model (blue), using the fracture pressurization from model 5 and considering a water level increase of 100 m. Horizontal displacement is positive when it is toward SE; vertical displacement is positive when upward. Black bar: mean noise level. Vertical displacement is positive when upward.

S3.3. Computation of the Coulomb failure function

We consider Coulomb stress change (CFF) in order to characterize the conditions for rock failure. It is defined on a fault plane as

$$CFF = \Delta\tau_r + \mu' \Delta\sigma_n \qquad \text{(S5)}$$

where $\Delta\tau_r$ is the change in the shear stress on the plane in the expected slip direction on the target fault, $\Delta\sigma_n$ is the change on normal stress (positive for extension) and μ' is the apparent coefficient of friction (Harris and Simpson, 1992), which we assumed = 0.5.

21

We compute $\Delta\tau_r$ and $\Delta\sigma_n$ starting from the three components of the stress tensor ($\Delta\sigma_{xx}$, $\Delta\sigma_{yy}$,$\Delta\sigma_{xy}$) obtained by the COMSOL model in a *x, y* reference frame, where *y* is vertical positive with elevation and *x* horizontal, positive toward SW.

Since the receiving faults we are considering are inverse:

$$\Delta\sigma_n = \Delta\sigma_{xx}\sin^2(\delta) - 2\Delta\sigma_{xy}(\sin(\delta)\cos(\delta)) + \Delta\sigma_{yy}\cos^2(\delta) \quad \text{(S6)}$$

$$\Delta\tau_r = \cos(\delta)\sin(\delta)(\Delta\sigma_{yy} - \Delta\sigma_{xx}) + \Delta\sigma_{xy}(\cos^2(\delta) - \sin^2(\delta)) \quad \text{(S7)}$$

Where δ is the dip angle.

Considering the high correlation between water storage changes, deformation and seismicity, with no significant time delay, pore pressure changes is not considered in the definition of CFF, and pore pressure changes won't be modeled.

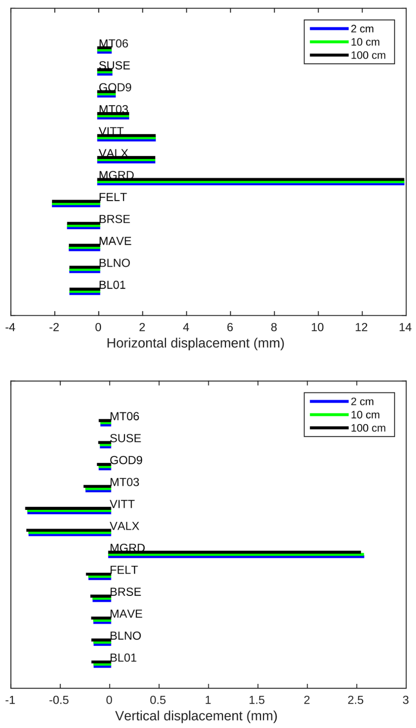

Figure S3.4. Horizontal (top) and vertical (bottom) displacements generated by the fracture described as Model 5, considering different values of initial opening: 2 cm (blue), 10 cm (green), 100 cm (black).

22

S4 Correlation between TWS_{res} and seismicity rates

S4.1 ETAS modelling and temporal declustering

- Completeness magnitude determination

The first step to investigate the possible correlation between the TWS_{res} and seismicity rate is to conduct statistical analysis on the seismic catalogue. Assessing the magnitude of completeness (Mc), defined as the minimum magnitude above which we have reliably recorded all the earthquakes in the time and the region under investigation is the first, essential step to analyse seismicity rates. Numerous algorithms for data-driven Mc selection have been proposed; Mignan and Woessner (2012) provide a quite exhaustive overview. To estimate Mc we use the "Completeness Magnitude Estimation" tool available on the IS-EPOS platform (IS-EPOS, 2016), which provides four different Mc estimations using different approaches (the goodness of fit at 90% and 95% confidence bounds, the Maximum Curvature Method (Wiemer, 2000) and the Modified Goodness of fit (Leptokaropoulos et al., 2013). The obtained Mc solutions are summarized in Table S4.1; since the value of 0.5 leads to unstable results, we adopt the more conservative value of $Mc=0.7$. The resulting complete catalogue is composed by 731 events.

Method	Mc
Goodness of fit test at 90% confidence bounds	0.5
Goodness of fit test at 95% confidence bounds	**0.7**
Maximum Curvature Method	0.5
Modified Goodness of fit test	**0.7**

Table S4.1. Summary of the Mc obtained using different methods (tools from IS-EPOS, 2016).

- Temporal declustering using the ETAS model

The seismic declustering consists in the identification and separation of the contribution of foreshocks, mainshocks and aftershocks, and to construct a catalogue composed only by independent events, i.e., those considered as not triggered by any preceding event. There are several approaches for solving the declustering problem, with a not unique solution. Van Stiphout et al. (2012) provides an overview of this issue, describing the pros and cons of the most popular algorithms. In this application, we adopt the strategy of Zhuang et al. (2002) which is based on the Epidemic Type Aftershock Sequence (ETAS) model. This model, firstly developed by Ogata (Ogata, 1988; 1998), considers the seismicity as the sum of background earthquakes thought to be caused by (stationary) tectonic loading and triggered earthquakes, thought to be caused by stress transfer. The stochastic declustering gives to each earthquake in the catalogue the probability of being an aftershock of all past events. Starting from the ETAS model, the conditional intensity, in the temporal domain, can be defined as:

$$\lambda_0(t) = \mu + \sum_{\{i:t_i<t\}} \frac{Ke^{\alpha(m-m_c)}}{(t-c)^p} \qquad \text{(S8)}$$

where μ represents the background events, that we assume time-independent; the cascade of aftershocks (in the summation) is described by the empirical Omori–Utsu law (Utsu et al., 1995), where k is the productivity factor of the sequence that depends on the magnitude (m) and $m_c$is the completeness magnitude. For the joint inversion of the five parameters for our complete catalogue, the maximum-likelihood method (Ogata et al., 1993) is used; we obtain: μ = 0.102 day−1, K = 0.025, α = 0.940, p = 0.907 and c = 0.226−2 yr.

For each event, it is possible to calculate the contribution to the background and the whole conditional intensity from equation (S8) and, from here, to select the most likely background events. We have found that 51% of the events are classified as background (372 earthquakes). The spatial distribution of these events is shown in Fig. 3a.

24

S4.2 Spatial cluster analysis

For spatial cluster analysis we use the k-means partitioning approach (MacQueen, 1967). This algorithm partitions a data set into k clusters so that the resulting intra-cluster similarity is high and the inter-cluster similarity is low (Han et al., 2011). We select the “optimal number of clusters” using the silhouette method (Rousseeuw, 1987), which is one of the most popular approaches used in literature (Kaufman and Rousseeuw, 1990; Al-Zoubi and Rawi, 2008; Garcia-Aristizabal et al., 2017). Fig. S4.1 shows the plot of the silhouette coefficient; the maximum of this plot, which is reached for k=2, indicates the preferred number of clusters to partition the data. In this way, the partition in two clusters (A and B in Fig. 3b) was obtained. It is worth noting that the classification of events located in the boundary between the two selected clusters may be discutible. To test the robustness of the obtained results we performed different tests in order to perform correlation analyses using resizing clusters A and B after manually changing the boundary between them (as e.g., following topographic features). These changes didn’t modified the resulting correlations between seismicity in the (modified) clusters A and B and TWS_{res}.

25

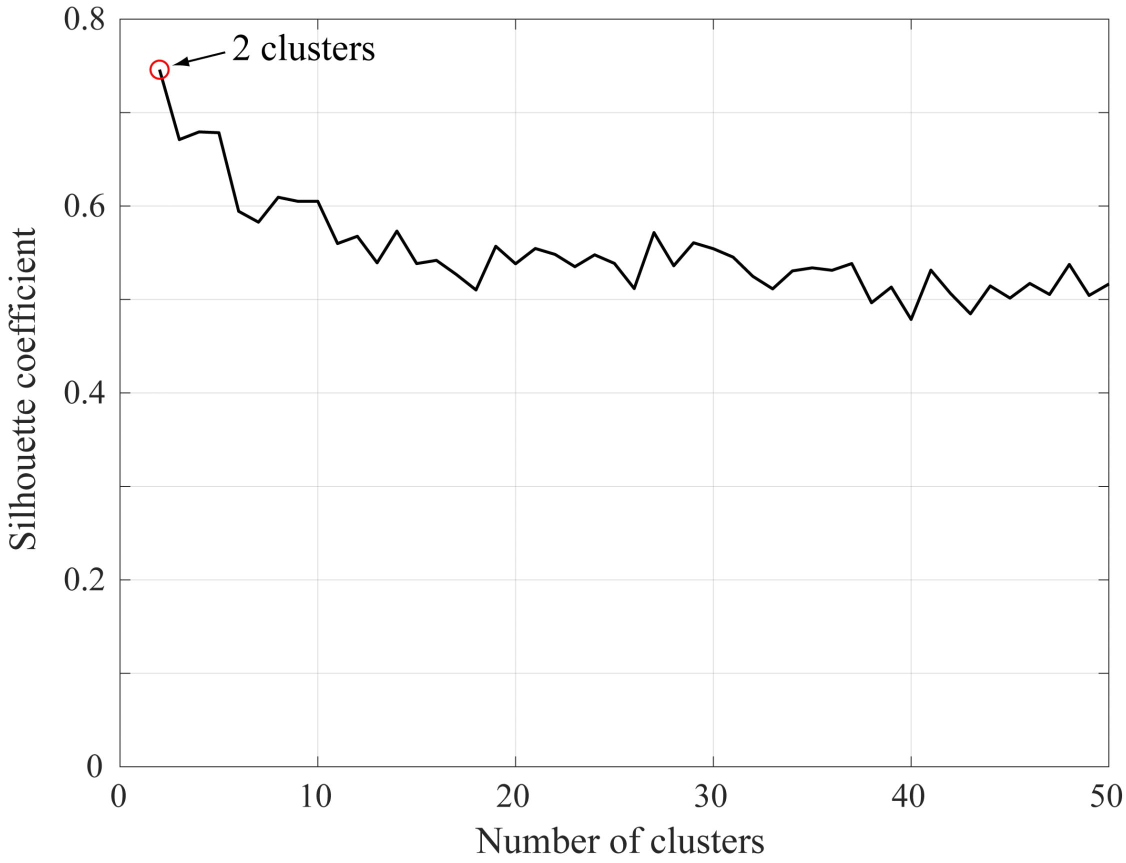

Figure S4.1. Plot of the mean Silhouette coefficient. The maximum value is found for a partition in two clusters (identified as clusters A and B in the paper).

S4.3 Covariate model

The covariate model from Garcia-Aristizabal (2018) provides a way for studying correlations between seismicity rates and proxies of possible forcing processes of interest. The exponential distribution is defined as the basic template function for modelling the t_{IET} as in equation (3). The possible dependencies on hydrological data are modelled writing the μ parameter of the exponential distribution in terms of deterministic functions of the explanatory covariate according to equation (4). The inference of model parameter values is performed using a Bayesian approach based on a Markov chain Monte Carlo (MCMC) method, whereas the model selection is based on Bayes factor (B_{KL}) calculations (Garcia-Aristizabal et al., 2015; 2016; 2018). B_{KL} provides a possible solution for hypothesis testing

26

and model selection in Bayesian inference problems (e.g. Kass and Raftery, 1995; Raftery, 1995; Lewis and Raftery, 1997) and is calculated as the ratio of the posterior odds for M_K against M_L to the prior odds. When the models M_K and M_L are *a priori* equally probable, B_{KL} reduces to the ratio of the marginal likelihoods of the two competing models (Lewis and Raftery, 1997) :

$$B_{KL} = \frac{f(x|M_K)}{f(x|B_L)} \quad \text{(S9)}$$

The Bayes factor summarizes the evidence provided by the data x in favour of one specific model as opposed to another. Reference values for interpreting B_{KL} have been provided by Jeffreys (1961) and Raftery (1995) and are summarized in Table S4.2 (from Garcia-Aristizabal, 2018).

$2\log_{10}(B_{KL})$	B_{KL}	**Evidence for M_K**
< 0	< 1	Negative (supports M_L)
0 - 2	1 - 3	Barely worth mentioning
2 - 5	3 - 12	Positive
5 - 10	12 - 150	Strong
> 10	> 150	Very strong

Table S4.2. Categories used for the interpretation of the Bayes factors for the model selection (from Raftery, 1995; Jeffreys, 1961; Garcia-Aristizabal, 2018).

We first analysed the full seismic catalog of background seismicity in the study area (Fig. 3a). Fig. S4.2 shows the moving average TWS_{res} and the rate of seismic events in the whole area (calculated in 90-days length time windows sliding at increments of 1 day). Testing the two competing models (stationary and log-linear) we find that the evidence provided by the Bayes factor is in favor of the stationary model (Table S4.3); this solution

27

indicates that a possible relationship between TWS_{res} and seismicity rates is not significant for this dataset. The parameter values of the competing models are summarized in Table S4.4. Tables S4.3 and S4.4 summarize also the Bayes factors and model parameter values obtained for the analysis considering the seismic data in spatial clusters A and B.

Dataset	B_{KL} **[K: log-linear; L: stationary]**	**Interpretation**
Full dataset	0.04	Negative (supports M_L)
Cluster A only	0.57	Negative (supports M_L)
Cluster B only	5.24	Positive

Table S4.3. Bayes factors calculated for model selection considering the full data set and the spatial clusters A and B.

28

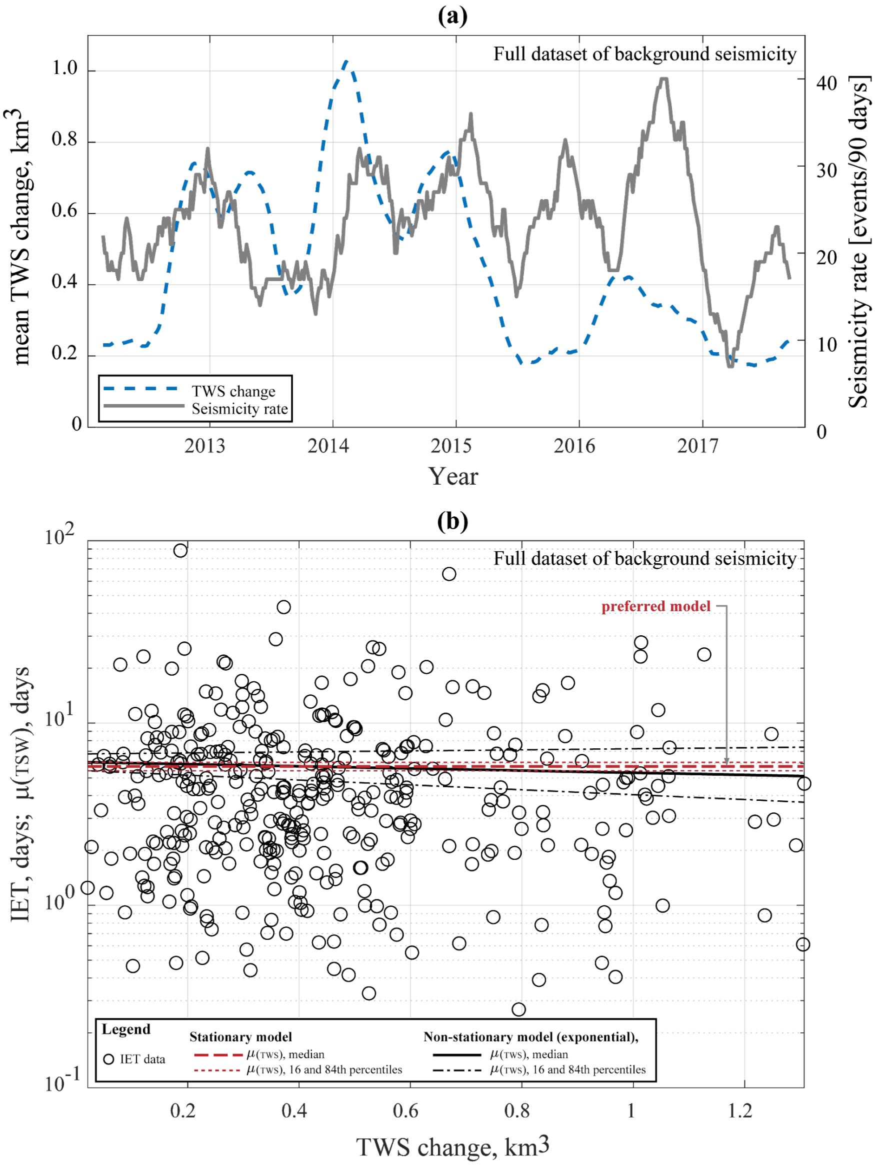

Figure S4.2. Moving average TWS_{res} (discontinuous line) and rate of the background seismicity identified in the full domain calculated in 90-days length time windows sliding at increments of 1 day.

 29

Dataset	Competing models from equation (4):	Parameter values median (16th, 84th percentiles)
Full dataset	**Stationary**	$\alpha_0 = 0.76\,(0.73, 0.78)$
	Log-linear	$\alpha_0 = 0.78\,(0.74, 0.83); \alpha_1 = -0.06\,(-0.13, 0.03)$
Cluster A	Stationary	$\alpha_0 = 0.99\,(0.96, 1.02)$
	Log-linear	$\alpha_0 = 0.93\,(0.88, 0.99); \alpha_1 = 0.12\,(0.03, 0.23)$
Cluster B	**Stationary**	$\alpha_0 = 1.14\,(1.11, 1.18)$
	Log-linear	$\alpha_0 = 1.28\,(1.21, 1.35); \alpha_1 = -0.29\,(-0.41, -0.17)$

Table S4.4. Model parameter values obtained for the competing models tested for assessing possible relationships between seismicity rates and TWS_{res} according to equation (4) (Stationary: $\log[\mu(x_{TWS})] = \alpha_0$; Log-linear: $\log[\mu(x_{TWS})] = \alpha_0 + \alpha_1 \cdot x_{TWS}$). The preferred model in each case is highlighted In bold.

V1 Supplementary video

In the top panel of the supplementary video V1 we show the temporal evolution of TWS_{res} (same as Fig. 4 in the maintext). In the bottom panel, the red segments connecting black dots and red dots represent the horizontal displacements associated with IC2 of each GNSS station. The displacements are calculated, as in section S1.2, with respect to the position at the instant corresponding to the absolute minimum of V2 (Fig. 4).

30

References

Al-Zoubi, M.B., Rawi, M., 2008. An efficient approach for computing silhouette coefficients. Journal of computer science 4, 252–255.

Altamimi, Z., Collilieux, X., Métivier, L., 2011. ITRF2008: an improved solution of the international terrestrial reference frame. J. Geod. 85, 457–473. doi:10.1007/s00190-011-0444-4

Anderlini, L., Serpelloni, E., Tolomei, C., De Martini, P.M., Pezzo, G., Gualandi, A., Spada, G., 2020. New insights into active tectonics and seismogenic potential of the Italian Southern Alps from vertical geodetic velocities. doi:10.5194/se-2020-10

Andermann, C., Longuevergne, L., Bonnet, S., Crave, A., Davy, P., Gloaguen, R., 2012. Impact of transient groundwater storage on the discharge of Himalayan rivers. Nature Geosci. 5, 127–132. doi:10.1038/ngeo1356

Anselmi, M., Govoni, A., De Gori, P., Chiarabba, C., 2011. Seismicity and velocity structures along the south-Alpine thrust front of the Venetian Alps (NE-Italy). Tectonophysics 513, 37–48. doi:10.1016/j.tecto.2011.09.023

Bevis, M., Brown, A., 2014. Trajectory models and reference frames for crustal motion geodesy. J. Geod. 88, 283–311. doi:10.1007/s00190-013-0685-5

Boehm, J., Heinkelmann, R., Schuh, H., 2007. Short Note: A global model of pressure and temperature for geodetic applications. J. Geod. 81, 679–683. doi:10.1007/s00190-007-0135-3

de Lavenne, A., Thirel, G., Andréassian, V., Perrin, C., Ramos, M.-H., 2016. Spatial variability of the parameters of a semi-distributed hydrological model. Proc. IAHS 373, 87–94. doi:10.5194/piahs-373-87-2016

Dong, D., Fang, P., Bock, Y., Cheng, M.K., Miyazaki, S., 2002. Anatomy of apparent seasonal variations from GPS-derived site position time series 107.

Dong, D., Fang, P., Bock, Y., Webb, F., Prawirodirdjo, L., Kedar, S., Jamason, P., 2006. Spatiotemporal filtering using principal component analysis and Karhunen-Loeve

31

expansion approaches for regional GPS network analysis. J. Geophys. Res. 111. doi:10.1029/2005JB003806

Dong, D., Herring, T.A., King, R.W., 1998. Estimating regional deformation from a combination of space and terrestrial geodetic data. J. Geod. 72, 200–214. doi:10.1007/s001900050161

Galadini, F., Poli, M.E., Zanferrari, A., 2005. Seismogenic sources potentially responsible for earthquakes with $M \geq 6$ in the eastern Southern Alps (Thiene-Udine sector, NE Italy). Geophys. J. Int. 161, 739–762. doi:10.1111/j.1365-246X.2005.02571.x

Garcia-Aristizabal, A., 2018. Modelling fluid-induced seismicity rates associated with fluid injections: examples related to fracture stimulations in geothermal areas. Geophys. J. Int. 215, 471–493. doi:10.1093/gji/ggy284

Garcia-Aristizabal, A., Bucchignani, E., Manzi, M.P., 2017. Patterns in Climate-Related Parameters as Proxy for Rainfall Deficiency and Aridity: Application to Burkina Faso. ASCE-ASME J. Risk Uncertainty Eng. Syst., Part A: Civ. Eng. 3, A4016001. doi:10.1061/AJRUA6.0000860

Garcia-Aristizabal, A., Bucchignani, E., Palazzi, E., D'Onofrio, D., Gasparini, P., Marzocchi, W., 2015. Analysis of non-stationary climate-related extreme events considering climate change scenarios: an application for multi-hazard assessment in the Dar es Salaam region, Tanzania. Nat. Hazards 75, 289–320. doi:10.1007/s11069-014-1324-z

Garcia-Aristizabal, A., Caciagli, M., Selva, J., 2016. Considering uncertainties in the determination of earthquake source parameters from seismic spectra. Geophys. J. Int. 207, 691–701. doi:10.1093/gji/ggw303

Gualandi, A., Serpelloni, E., Belardinelli, M.E., 2016. Blind source separation problem in GPS time series. J. Geod. 90, 323–341. doi:10.1007/s00190-015-0875-4

Han, J., Kamber, M., Pei, J., 2011. Data mining concepts and techniques third edition. Morgan Kaufmann.

Harris, R.A., Simpson, R.W., 1992. Changes in static stress on southern California faults after the 1992 Landers earthquake. Nature 360, 251–254. doi:10.1038/360251a0

32

IS-EPOS. 2016. *Completeness Magnitude Estimation* [Web application/Source code]. Retrieved from https://tcs.ah-epos.eu/

Jeffreys, H., 1961. Theory of probability, 3rd edn oxford: Oxford university press.

Jensen, M.E., Burman, R.D., Allen, R.G., 1990. Evapotranspiration and irrigation water requirements.

Kass, R.E., Raftery, A.E., 1995. Bayes Factors. J. Am. Stat. Assoc. 90, 773–795. doi:10.1080/01621459.1995.10476572

Kaufman, L., Rousseeuw, P.J. (Eds.), 1990. Partitioning around medoids (program PAM), in: Finding Groups in Data, Wiley Series in Probability and Statistics. John Wiley & Sons, Inc., Hoboken, NJ, USA, pp. 68–125. doi:10.1002/9780470316801.ch2

Lagler, K., Schindelegger, M., Böhm, J., Krásná, H., Nilsson, T., 2013. GPT2: Empirical slant delay model for radio space geodetic techniques. Geophys. Res. Lett. 40, 1069–1073. doi:10.1002/grl.50288

Leptokaropoulos, K.M., Karakostas, V.G., Papadimitriou, E.E., Adamaki, A.K., Tan, O., Inan, S., 2013. A homogeneous earthquake catalog for western turkey and magnitude of completeness determination. Bulletin of the Seismological Society of America 103, 2739–2751. doi:10.1785/0120120174

Lewis, S.M., Raftery, A.E., 1997. Estimating Bayes Factors via Posterior Simulation with the Laplace—Metropolis Estimator. J. Am. Stat. Assoc. 92, 648–655. doi:10.1080/01621459.1997.10474016

Longuevergne, L., Florsch, N., Boudin, F., Oudin, L., Camerlynck, C., 2009. Tilt and strain deformation induced by hydrologically active natural fractures: application to the tiltmeters installed in Sainte-Croix-aux-Mines observatory (France). Geophys. J. Int. 178, 667–677. doi:10.1111/j.1365-246X.2009.04197.x

Lyard, F., Lefevre, F., Letellier, T., Francis, O., 2006. Modelling the global ocean tides: modern insights from FES2004. Ocean Dynamics 56, 394–415. doi:10.1007/s10236-006-0086-x

MacQueen, J., 1967. Some methods for classification and analysis of multivariate observations. Proceedings of the fifth Berkeley symposium on mathematical statistics and probability 1, 281–297.

Mignan, A., Woessner, J., 2012. Estimating the magnitude of completeness for earthquake catalogs. Community Online Resource for Statistical Seismicity Analysis. doi:10.5078/corssa-00180805

Nash, J.E., Sutcliffe, J.V., 1970. River flow forecasting through conceptual models part I — A discussion of principles. J Hydrol (Amst) 10, 282–290. doi:10.1016/0022-1694(70)90255-6

Ogata, Y., 1988. Statistical Models for Earthquake Occurrences and Residual Analysis for Point Processes. J. Am. Stat. Assoc. 83, 9–27. doi:10.1080/01621459.1988.10478560

Ogata, Y., 1998. Space-Time Point-Process Models for Earthquake Occurrences. Ann. Inst. Stat. Math. 50, 379–402. doi:10.1023/A:1003403601725

Ogata, Y., Matsu'ura, R.S., Katsura, K., 1993. Fast likelihood computation of epidemic type aftershock-sequence model. Geophys. Res. Lett. 20, 2143–2146. doi:10.1029/93GL02142

Oudin, L., Hervieu, F., Michel, C., Perrin, C., Andréassian, V., Anctil, F., Loumagne, C., 2005. Which potential evapotranspiration input for a lumped rainfall–runoff model? J Hydrol (Amst) 303, 290–306. doi:10.1016/j.jhydrol.2004.08.026

Petrie, E.J., King, M.A., Moore, P., Lavallée, D.A., 2010. Higher-order ionospheric effects on the GPS reference frame and velocities. J. Geophys. Res. 115. doi:10.1029/2009JB006677

Pushpalatha, R., Perrin, C., Le Moine, N., Mathevet, T., Andréassian, V., 2011. A downward structural sensitivity analysis of hydrological models to improve low-flow simulation. J Hydrol (Amst) 411, 66–76. doi:10.1016/j.jhydrol.2011.09.034

Raftery, A.E., 1995. Hypothesis testing and model. Markov chain Monte Carlo in practice 165–187.

Rodell, M., 2016. GLDAS Noah Land Surface Model L4 monthly 0.25 x 0.25 degree, Version 2.1. NASA Goddard Earth Sciences Data and Information Services Center. doi:10.5067/sxavczfaqlno

Rousseeuw, P.J., 1987. Silhouettes: A graphical aid to the interpretation and validation of cluster analysis. Journal of Computational and Applied Mathematics 20, 53–65. doi:10.1016/0377-0427(87)90125-7

Schmid, R., Rothacher, M., Thaller, D., Steigenberger, P., 2005. Absolute phase center corrections of satellite and receiver antennas. GPS Solut. 9, 283–293. doi:10.1007/s10291-005-0134-x

Schmid, R., Steigenberger, P., Gendt, G., Ge, M., Rothacher, M., 2007. Generation of a consistent absolute phase-center correction model for GPS receiver and satellite antennas. J. Geod. 81, 781–798. doi:10.1007/s00190-007-0148-y

Serpelloni, E., Casula, G., Galvani, A., Anzidei, M., Baldi, P., 2006. Data analysis of Permanent GPS networks in Italy and surrounding region: application of a distributed processing approach. Annals of Geophysics.

Serpelloni, E., Faccenna, C., Spada, G., Dong, D., Williams, S.D.P., 2013. Vertical GPS ground motion rates in the Euro-Mediterranean region: New evidence of velocity gradients at different spatial scales along the Nubia-Eurasia plate boundary. J. Geophys. Res. Solid Earth 118, 6003–6024. doi:10.1002/2013JB010102

Serpelloni, E., Vannucci, G., Anderlini, L., Bennett, R.A., 2016. Kinematics, seismotectonics and seismic potential of the eastern sector of the European Alps from GPS and seismic deformation data. Tectonophysics 688, 157–181. doi:10.1016/j.tecto.2016.09.026

Utsu, T., Ogata, Y., S, R., Matsu’ura, 1995. The Centenary of the Omori Formula for a Decay Law of Aftershock Activity. J,Phys,Earth 43, 1–33. doi:10.4294/jpe1952.43.1

van Stiphout, T., Marsan, D., Zhuang, J., 2012. Seismicity declustering. Community Online Resource for Statistical Seismicity Analysis. doi:10.5078/corssa-52382934

Wiemer, S., 2000. Minimum Magnitude of Completeness in Earthquake Catalogs: Examples from Alaska, the Western United States, and Japan. Bulletin of the

Seismological Society of America 90, 859–869. doi:10.1785/0119990114

Zhuang, J., Ogata, Y., Vere-Jones, D., 2002. Stochastic Declustering of Space-Time Earthquake Occurrences. J. Am. Stat. Assoc. 97, 369–380.S., 2000. doi:10.1198/016214502760046925

36